In Vivo Inspection of the Olfactory Epithelium: Feasibility of Robotized Optical Biopsy

CÉDRIC GIRERD [iD],[1] THOMAS LIHOREAU,[5] KANTY RABENOROSOA,[2] BRAHIM TAMADAZTE,[2]
MOURAD BENASSAROU,[4] LAURENT TAVERNIER,[3] LIONEL PAZART,[5] EMMANUEL HAFFEN,[5]
NICOLAS ANDREFF,[2] and PIERRE RENAUD[1]

[1]AVR-ICube, CNRS, Université de Strasbourg, INSA Strasbourg, 1 Place de l'Hôpital, 67000 Strasbourg, France; [2]FEMTO-ST Institute, Univ. Bourgogne Franche-Comté/CNRS, Besançon, France; [3]Univ. Hospital of Besançon, Univ. Bourgogne Franche-Comté, 3 bd Alexandre Fleming, 25030 Besançon, France; [4]La Pitié Salpêtrière Hospital, 47-83 Boulevard de l'Hôpital, 75013 Paris, France; and [5]CIC Inserm 1431, Univ. Hospital of Besançon, Univ. Bourgogne Franche-Comté, 3 bd Alexandre Fleming, 25030 Besançon, France

Associate Editor Cameron N. Riviere oversaw the review of this article.

Abstract—Inspecting the olfactory cleft can be of high interest, as it is an open access to neurons, and thus an opportunity to collect *in situ* related data in a non-invasive way. Also, recent studies show a strong link between olfactory deficiency and neurodegenerative diseases such as Alzheimer and Parkinson diseases. However, no inspection of this area is possible today, as it is very difficult to access. Only robot-assisted interventions seem viable to provide the required dexterity. The feasibility of this approach is demonstrated in this article, which shows that the path complexity to the olfactory cleft can be managed with a concentric tube robot (CTR), a particular type of continuum robot. First, new anatomical data are elaborated, in particular for the olfactory cleft, that remains hardly characterized. 3D reconstructions are conducted on the database of 20 subjects, using CT scan images. Measurements are performed to describe the anatomy, including metrics with inter-subject variability. Then, the existence of collision-free passageways for CTR is shown using the 3D reconstructions. Among the 20 subjects, 19 can be inspected using only 3 different robot geometries. This constitutes an essential step towards a robotic device to inspect subjects for clinical purposes.

Keywords—Olfactory epithelium, ENT, Robot-assisted intervention, Continuum robot, OCT.

Address correspondence to Cédric Girerd, AVR-ICube, CNRS, Université de Strasbourg, INSA Strasbourg, 1 Place de l'Hôpital, 67000 Strasbourg, France. Electronic mail: cedric.girerd@insa-strasbourg.fr

INTRODUCTION

There is a growing interest in the study of the olfactory epithelium (OE) (Fig. 1). It is the most proximal axonal area of the human brain, with neurons that can be regenerated.[12] Its *in vivo* analysis is considered in neuroscience for brain medicine development.[14,28] Both nasal cavities of a subject are known to have functional differences, as illustrated in Ref. 5, which are interesting to investigate. In neurology, several recent clinical studies[13,21,22,26] have demonstrated the existence of a correlation between the appearance of neurodegenerative diseases and the loss of smell. This latter could therefore be a reliable precursor sign of neuronal degeneration, before memory and motricity deficiency signs.[17] Alzheimer and other dementias are projected to show a 66% increase from 2005 to 2030.[1] Confirmation of the occurrence of OE neuropathological changes for neurodegenerative diseases is then of utmost interest, which requires direct and objective exploration of the OE.

New contactless imaging modalities like optical coherence tomography (OCT) can provide 3D optical biopsies, with a spatial resolution that is adapted to the individual size of the olfactory cells, typically in the order of a few tens of micrometers in diameter.[18] Such a modality can in addition make use of an optical fiber-based probe. The fiber can be associated to a prism, to orientate the light ray and thus make a side-firing probe. They can have a diameter as low as 0.125 μm, and are available today at a commercial level.[3] Thus,
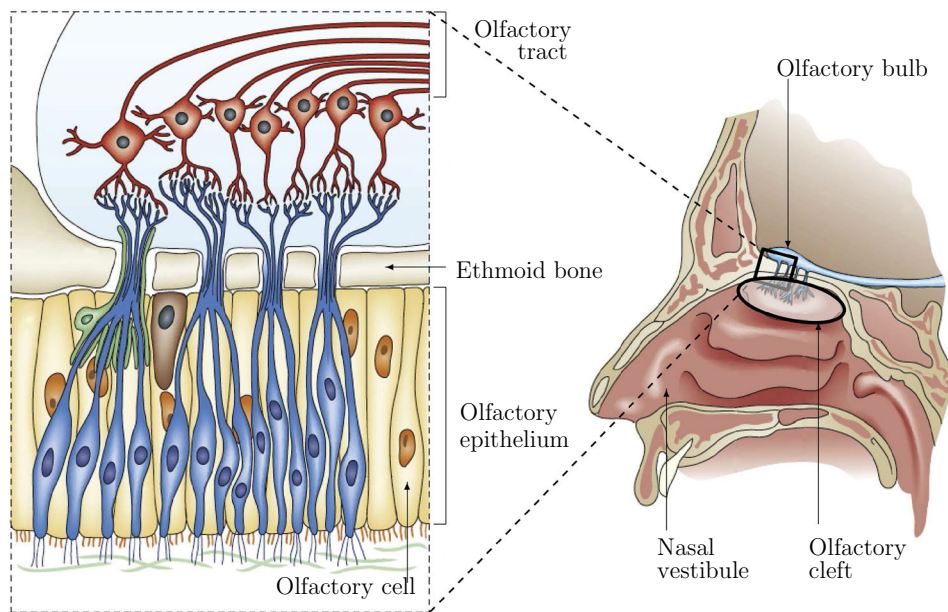
FIGURE 1. Illustration adapted from Ref. 20 of the olfactory mechanism and the related anatomy, with a global view of the nasal cavity on the right and a detailed view of the tissues that cover the roof of the olfactory cleft on the left.

an imaging technique for *in situ* observation of the OE is no longer an issue.

On the contrary, *in vivo* observation of the OE is still an open challenge because of its location and access. Bringing the imaging probe to the OE requires to go inside the olfactory cleft (Fig. 1), a hollow structure of well-known geometrical complexity.[31] The OE covers the olfactory clefts (Fig. 1), which length is about 30 mm, with a dense distribution of neural receptors right after its entry.[27] However, the width of the olfactory cleft does not exceed 2 mm. The size of the probe-holder is therefore strongly constrained. In addition, no conventional instrument can be used to reach non-invasively this area. Their size and straight shape make them incompatible with the geometry of the olfactory cleft. Finally, the OE inspection requires fine scanning motions, of resolution compatible with the olfactory cells size and imaging technology. A manual approach does not seem adapted in this context. In our opinion, only a robotized approach is viable. It has indeed been considered successfully in several medical applications with close constraints.[6,9,10,23,32] Several types of continuum robots have been demonstrated to be of interest for navigation in the human body,[8] and are then being used to overcome limitations of manual approaches with conventional instruments. Concentric tube robots (CTR) are indeed particularly relevant in the present context. Such robots are an assembly of superelastic precurved tubes, that interact and conform to give the robot its shape. The latter can be changed by relative translations and rotations of the individual tubes. The absence of active elements inside the robot maximizes the compactness, with achievable diameters below 1 mm.[15,33] Such continuum robots can in addition be deployed in a so-called follow-the-leader (FTL) manner, during which the backbone of the robot follows the path traced out by its tip.[19] This means that the robot occupies a minimal volume during its deployment. It is a particularly interesting deployment strategy in highly constrained environments such as the nasal cavity. We therefore consider that it is of utmost interest to assess the feasibility of a robotized inspection using a CTR with FTL deployment for *in situ* characterization of olfactory cells, to be used for clinical purposes.

As described above, the key issues are related to the absence of straight access to the OE and the very limited space available in the nasal cavity. The feasibility of a robot-assisted *in vivo* inspection of the OE is therefore intrinsically linked to the determination of deployment schemes of a robotic device that are compatible with the human anatomy. In this paper, we demonstrate, using engineering techniques applied to medicine, that it is possible to inspect the OE with a rather simple approach, despite the complexity of the nasal cavity.

The problem in this determination is twofold. First, there is very limited information on the olfactory cleft geometry in the literature. 3D information, here mandatory to assess the robotic approach feasibility, is not available. Inter-subject variability is *a priori*

significant, and needs to be assessed, including potential differences between left and right cavities for a single subject. Second, deployment paths have to be generated to verify the existence of robotized solutions to inspect the OE. The corresponding methodologies and results are presented in ''Materials and Methods'' and ''Results'' respectively, followed by a discussion in ''Discussion''.

MATERIALS AND METHODS

Our general approach is to decompose the analysis in two steps. First, 3D information on the geometry of the nasal cavity, including the olfactory cleft is established. Second, the existence of admissible paths for a robotic device is assessed. The anatomy of the nostril is complex, being composed of soft tissues in the nasal vestibule area (Fig. 1), and then of bone and cartilage in the upper part. Given the rigidity of the latter elements, no contact or interaction with them is admissible. In the olfactory cleft, the mucosa that covers the OE cannot be in contact with a device either, because of its fragility. We therefore need the 3D shape of the nasal cavity corresponding to these structures, including inter-subject variability. To do so, a set of 20 subjects (10 females, 10 males) aged 18 or more is selected for our study. In order to maximize the reconstruction accuracy for our study, CT images are being considered. According to the regulatory requirements for this kind of research, a study protocol entitled "Evaluation of inter-patient variability of the nasal cavity dimensions from CT scans" was established. This protocol, as well as patient information leaflet (for information and non-opposition) and regulatory forms, were declared to the French commission for data protection *"Commission nationale de l'informatique et des libertés"* (CNIL). The authorization of study set up, represented by the declaration receipt, was received on December 24th, 2015. Following the protocol, CT scans of 20 patients from a SIEMENS SOMATOM Definition AS + scanner were chosen by maxillofacial surgeons of the University Hospital of Besançon. Selected subjects are adults with fully formed nasal cavities that no longer experience structural and morphological changes. In their selection, the surgeons avoided profiles presenting any pathology that could interfere with the targeted parameters of the study in the concerned area (sinusitis, cancer, previous surgeries for instance). The files were subsequently anonymized. Images are taken in transverse planes, with resolutions in the range of 0.25–0.39 mm, and slice thickness between 0.6 and 1.0 mm.

As mentioned earlier, information on the olfactory cleft anatomy is not available in the literature. The most interesting results are presented in Refs. 16 and 34, where medical images are used to perform a set of measurements. However, the methodologies used to obtain these results are not suitable to our needs, first because measurements are performed in conventional anatomical planes. Distance measurements can be biased since these planes do not correspond necessarily to the principal planes of the evaluated geometry. Second, only local measurements are performed, that are not sufficient to establish the admissibility of a robotic deployment. On the contrary, the results we present are based on whole 3D reconstructions of the nasal cavity anatomy.

The reconstruction process is composed of three steps, namely segmentation, 3D reconstruction and extraction of the area of interest, as illustrated in Fig. 2. On the contrary to approaches such as described by Bui,[7] a manual threshold-based method is used for segmentation. It allows a manual selection of greyscale levels, after visual inspection of the images by an operator to delimit the air/tissue interface. Such approach is considered since grey level corresponding to the tissues is dependent on the subject and no standard setting can be adopted. The impact of the user choice on the accuracy of the tissue location was estimated by asking 10 users to determine the threshold for a same subject. These 10 users had no medical background, so the estimation tends to be an upper bound of the measurement error. The impact of the threshold variability was then assessed by comparing the mesh reconstructed using the mean threshold, and the same shifted with the observed standard deviation. The root mean square (RMS) shape difference in the area of interest is equal to 0.04 mm. Such accuracy in the determination of this interface is hence considered satisfactory.

The segmentation and 3D reconstructions steps are performed using InVesalius,[2] which implements a Marching Cubes algorithm[29] and a context-aware smoothing algorithm[30] used for our application. The extraction of the nasal cavity is performed using Meshlab.[11] The final result is a set of 40 meshes of nasal cavities, two for each subject. An example of left and right nasal cavities is represented in Fig. 2.

From this set of meshes, the assessment of the robot-assisted inspection feasibility can be performed. CTR are a particular type of continuum robots, able to follow a path in a FTL manner when this latter is composed of constant-curvature segments.[4,19] A representation of a CTR is visible in Fig. 3a. In the following, we designate segments and links as the constant-curvature portions of the path to follow and of the robot, respectively (Fig. 3b). Concentric tube robots that are planar and made of constant curvature tubes are compatible with a FTL deployment,[19] as long
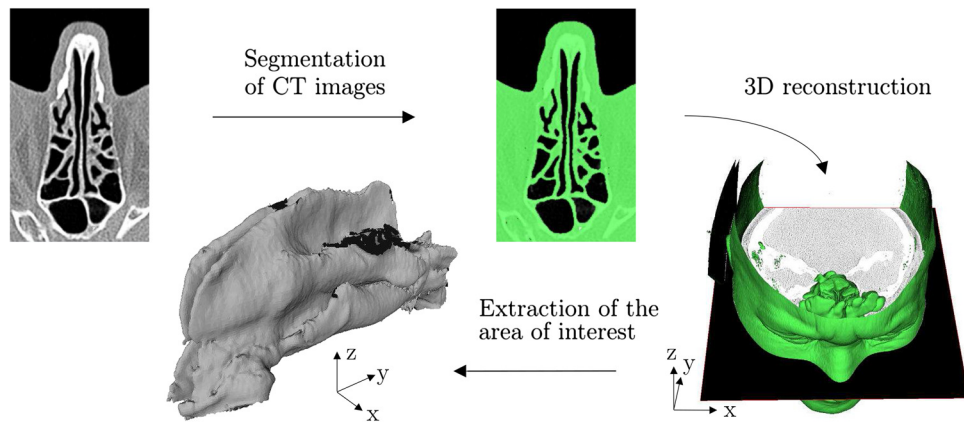
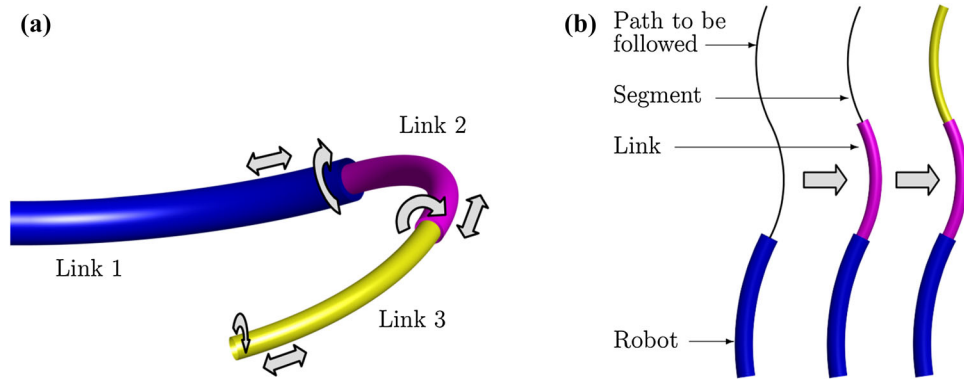**FIGURE 2.** Reconstruction process of the nasal cavity.

FIGURE 3. (a) CTR distal end, with 3 tubes that can be rotated and translated relatively to one another; and (b) FTL deployment sequence for such CTR.

as the robot is not subject to external loads. In this case, corresponding to our context, its deployed shape is considered as composed of a sequence of constant-curvature links of cylindrical shapes, each one of a specific diameter. Determination of feasible solutions consists in identifying the curvature, diameter of the constant-curvature links to reach the OE, as well as their curvilinear lengths.

Based on the robotic task division introduced in other contexts,[4,25] two functional sections are introduced for the CTR. The first one aims at reaching the olfactory cleft entry, designated in the following as the navigation task, with a dedicated navigation section (Fig. 4). The second one aims at scanning the OE, which is the exploration task, realized by an exploration section. Selection of the number of links can be performed by considering each of these two tasks. Since the maximum outer diameter of a CTR is directly linked to the number of links, it is desired to minimize this number given the strong space constraints. A single constant-curvature link for the navigation section is not sufficient given the anatomy. Two constant-curvature links are at least needed for the navigation

section. The nasal vestibule is actually reached today with straight conventional tools. Based on this information, the first link is thus chosen straight, while the second segment is chosen curved, with a curvature to be determined. For the exploration section, a straight link is selected for simplicity. The shape of the robot is therefore parameterized by the length of the straight, curved links of the navigation section, denoted l_1 and l_2 respectively, by the length l_3 of the straight link of the exploration section, and by the curvature c_2 of the curved link of the navigation section (Fig. 4).

The deployment and scanning tasks can be defined as follows. During the exploration task, the distance between the robot tip and the roof must remain in the range of [2,4] mm in order to image the OE. Therefore, one extremity of the curve describing the navigation section has to be placed at a distance of 3 mm, the average distance, to the roof of the olfactory clefts (Fig. 4). A frame (x_1, y_1, z_1) is defined accordingly. Its orientation is obtained by rotating the base frame about the z_0 and x_0 axis, so that the y_1 axis is centered between the olfactory cleft lateral surfaces, and is parallel to its roof. The tangent to the curve describing
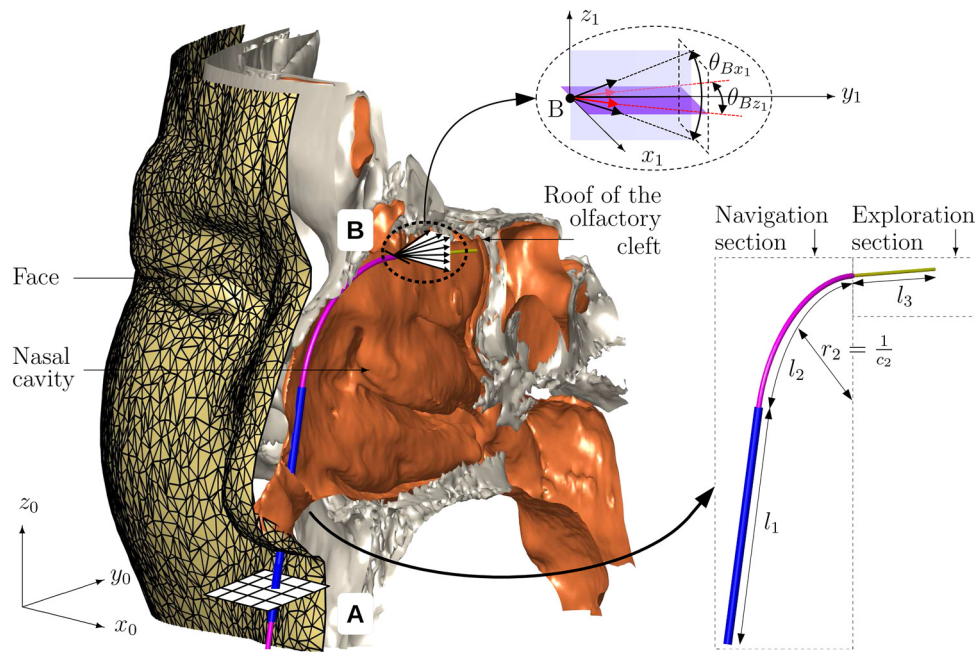
FIGURE 4. Parameterization of the navigation and exploration sections of the CTR for the inspection of the olfactory epithelium.

the navigation section is set parallel to the roof of the olfactory cleft to ease the deployment of the exploration section of the robot, with orientation tolerances of 10 degrees of amplitude about the x_1 and z_1 axes, designated by angles θ_{Bx_1} and θ_{Bz_1} respectively as illustrated in Fig. 4 to account for the [2,4] mm of distance to the OE. Some flexibility exists in the positioning of the robot base with respect to the nasal cavity. This placement freedom is used to maximize the chance of finding a collision-free navigation section. The geometry chosen to go from the nostril to the entry point of the olfactory cleft is parameterized by the location of the entry point A (Fig. 4), of the final point B, and the orientation in point B, for the deployment of the exploration section. The position of point A in the xy plane (Fig. 4) is defined by the coordinates x_A and y_A. Similarly, point B can be modified along the x axis (Fig. 4), and x_B designates its location.

The search for admissible deployment paths for the robot is then achieved by exhaustive exploration of the solution space obtained after a discretization. First, a discretization of the three variables (x_A, y_A, x_B) is performed, with a discretization step of 1 mm for the coordinates of point A and 0.25 mm for the coordinate of point B, as it is located in a more constrained area. The orientation tolerances are discretized as well, with an angular step size of 2 degrees for θ_{Bx_1} and θ_{Bz_1}. Then, all the combinations of x_A, y_A, x_B, θ_{Bx_1}, θ_{Bz_1} and c_2 are generated. For each of them, a collision test is performed with each of the 40 nasal cavities, with the

criterion that no contact should occur, except with the soft tissue of the nostril. Given the large number of evaluations to be performed, a computational-efficient implementation is needed. Thus, parallelization is adopted with the Parallel Computing Toolbox of Matlab (The MathWorks Inc., Natick, USA), and the V-Collide[24] library is used to assess the collision occurrence efficiently. The deployment of an exploration section is not possible if no navigation section can reach the olfactory cleft entry. Therefore, only the admissible solutions for the navigation section are considered for determination of the exploration section. A straight exploration segment is added at the distal end of the navigation section. Its length is increased progressively, with a step size of 1 mm, and for each step size, the occurrence of collision with each nasal cavity of the 20 subjects is assessed.

RESULTS

Five main anatomical observations can be made directly from the obtained set of meshes.

First, large deviations of the nasal septum can be observed for some subjects, a phenomenon well-known by ENT surgeons. Figure 5a illustrates this feature on one of the 3D reconstructed models. Similarly, the olfactory clefts are not located in a single plane. A bending is observed with deviations from the sagittal plane, as illustrated in Fig. 5b.
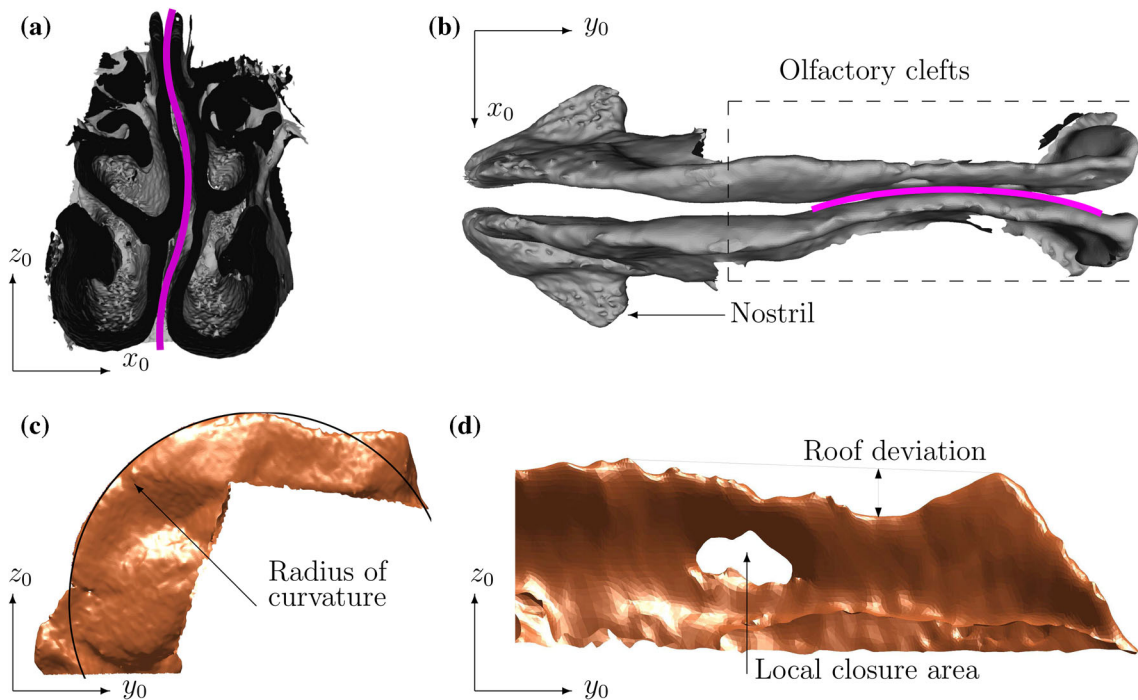
FIGURE 5. Direct observations on the reconstructed data: observed non-planarities of the nasal cavities, with (a) the deviation of the nasal septum; (b) the deviation of the olfactory cleft; (c) curvature measurement of the anterior part of the nasal cavity; and (d) illustration of the deviation of the olfactory cleft roof, with an example of local closure. Magenta lines in (a) and (b) outline the deviation of the anatomical areas.

The second piece of information concerns the overall shape of the nasal vestibule. The anterior part of the nasal vestibule has a curved shape. Its geometry can be described by extracting the points located on the anterior edge, and then fitting an arc, as illustrated in Fig. 5c. The minimum, maximum and RMS radius of curvature are 21.3, 58.6 and 39.4 mm, respectively. Such values constrain admissible geometries of a robot, since it can navigate close to this area to reach the olfactory cleft.

Third, the side surfaces of the olfactory clefts occasionally fusion locally, as illustrated in Fig. 5d. Such closures occur in 10 out of the 40 cases. This is an important feature, as it means that no direct observation of the OE can be achieved around these regions.

Fourth, it is clear thanks to the 3D reconstructions that the roofs of the olfactory clefts are not flat. Therefore, if the imaging probe follows a straight trajectory, the distance between this probe and the area to be scanned will vary. Maximum deviations of the roof of the olfactory cleft are computed as represented in Fig. 5d. Minimum, maximum and RMS deviation values are equal to 0.3, 6.4 and 2.7 mm, respectively, which again constrain possible robot shapes to gain access to the OE.

Finally, thanks to the 3D reconstructions, it is possible to compute the evolution of the nasal cavity width. To do so, points on one of the surfaces of the nasal cavity are selected. In the nasal vestibule, and as illustrated in Fig. 6a, the selection has a rectangular-like shape that connects the nostril to the olfactory cleft entry. In the olfactory cleft, the points are located at a minimum distance of 2 mm to its roof, and a maximum distance of 4 mm. For each point, the distance to the other surface is computed using a point-to-surface measurement algorithm. The corresponding closest points are represented in Fig. 6a in blue for the nasal vestibule, and magenta for the olfactory cleft. In the nasal vestibule, the measured widths are greater than 2 mm as represented in Fig. 6b. A second path is then built parallel to the roof of the olfactory cleft, starting from its entry point. Given the goal of holding an OCT imaging probe, we consider an offset distance in the range of 2 to 4 mm with respect to the olfactory cleft roof. Distances between the lateral surfaces of the nasal cavity are computed along this path, using the same technique, as illustrated in Fig. 6a. Figure 6b represents the evolution of the nasal cavity width along the passageway. It is visible that the width of the nasal cavity tends to decrease along the path. From our previous observations and regarding the plot of the width against the path length, we can see that the most constrained area where the robot will navigate is the olfactory cleft, with width values between 1 and 2 mm.
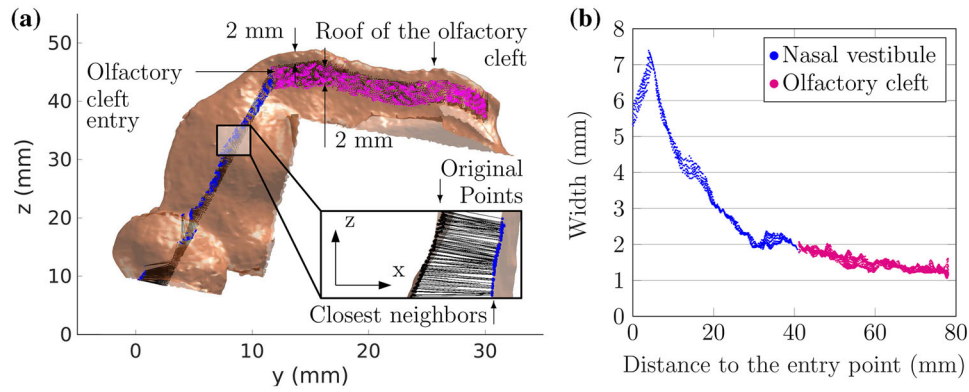
FIGURE 6. (a) side view of the areas of measurement of the nasal vestibule (blue) and the olfactory cleft (magenta); and (b) evolution of the width of the nasal cavity along the identified points.

Also, the dispersion of the measurements for a given position on the passageway is very low: there are no important changes in the width of the nasal cavity as we come closer or move away from the roof of the olfactory cleft.

Access with a robotic device is mostly constrained in terms of size by the width of the olfactory cleft. As a consequence, inter-subject variability is assessed for this region in particular. The presented point-to-surface measurement methodology is applied in this area for the 20 subjects. When encountered, closure areas of the olfactory clefts are excluded from the measurements. Only 0.05% of the width distribution is below a value of 1 mm. Figure 7 is a boxplot representing the width distribution for the individual nasal cavities of each subject. Subject from number 1 to 10 represent women, and subjects from 11 to 20 represent men. Also, Table 1 provides simplified statistical data for the entire dataset of 20 subjects. It is visible that the width of the olfactory clefts is lower than 1 mm for 3 subjects only, and for a very limited number of situations. The 1-mm threshold is therefore considered as the maximum robot diameter in that area.

The previous observations and measurements give us the ability to assess the robot deployment paths. We observed that the nasal vestibule is non-planar. The out-of-plane variations are taken into account by choosing a cylindrical shape of diameter lower than the identified width of the nasal cavity. More precisely, the segment diameters are chosen equal to 1.6 and 1.0 mm, respectively, for the straight and curved segments, which gives us at least 1 mm of gap with respect to the nasal cavity width. For the exploration section, a diameter of 0.65 mm is chosen. This diameter, lower than the 1-mm value identified hereabove, is aimed at allowing a straight deployment even though the olfactory clefts are not perfectly planar. Given the computed anatomical data, admissible values for this parameter are set in the interval of [0.02 0.09] mm^{-1},

with a discretization step of 0.01 mm^{-1}. The combinations of x_A, y_A, x_B, θ_{Bx}, θ_{Bz} and c_2 lead to approximately 1 million candidate robots to assess per nasal cavity.

The number of solutions for each nasal cavity can vary, as illustrated in Figs. 8a and 8b, with 950 and 3 solutions, respectively. For each subject, the minimum and maximum lengths of link 1 and 2 are determined from all the set of admissible solutions for the corresponding subject, and are reported on Table 2. 19 out of 20 subjects can be inspected, which corresponds to a success rate of 95%. Even more interestingly, a single curvature makes a high inspection rate possible: 18 out of 20 subjects can be inspected with a curvature of 0.04 mm^{-1} for the distal segment, which gives a success rate of 90%. Considering in addition curvatures of 0.03 and 0.05 mm^{-1} gives access to 1 more subject and 7 additional nasal cavities. This demonstrates that the olfactory cleft can be reached for a significant number of subjects. Also, both nasal cavities of a subject can be accessed for a significant number of cases with all 3 different curvatures combined (16 out of 20 subjects).

There are 7928 out of 1 million tested combinations that are admissible for all the nasal cavities during the determination of the navigation section. The exploration section is computed only for the navigation sections that can successfully reach the entry of the olfactory cleft, without collision. The minimum and maximum deployable lengths of the exploration section are reported on Table 2 for each nasal cavity. This corresponds to the olfactory cleft portion that can be imaged. For the curvature of 0.04 mm^{-1} that leads to the highest rate of inspected subjects, the mean deployable length for all subjects is equal to 10.4 mm, which is 35% of the total length of the olfactory cleft. These satisfactory results consolidate the relevant choice of a CTR made of 3 links. A lower number of sections would have lead to a robot incompatible with the observed shape of the nasal cavity, and a higher
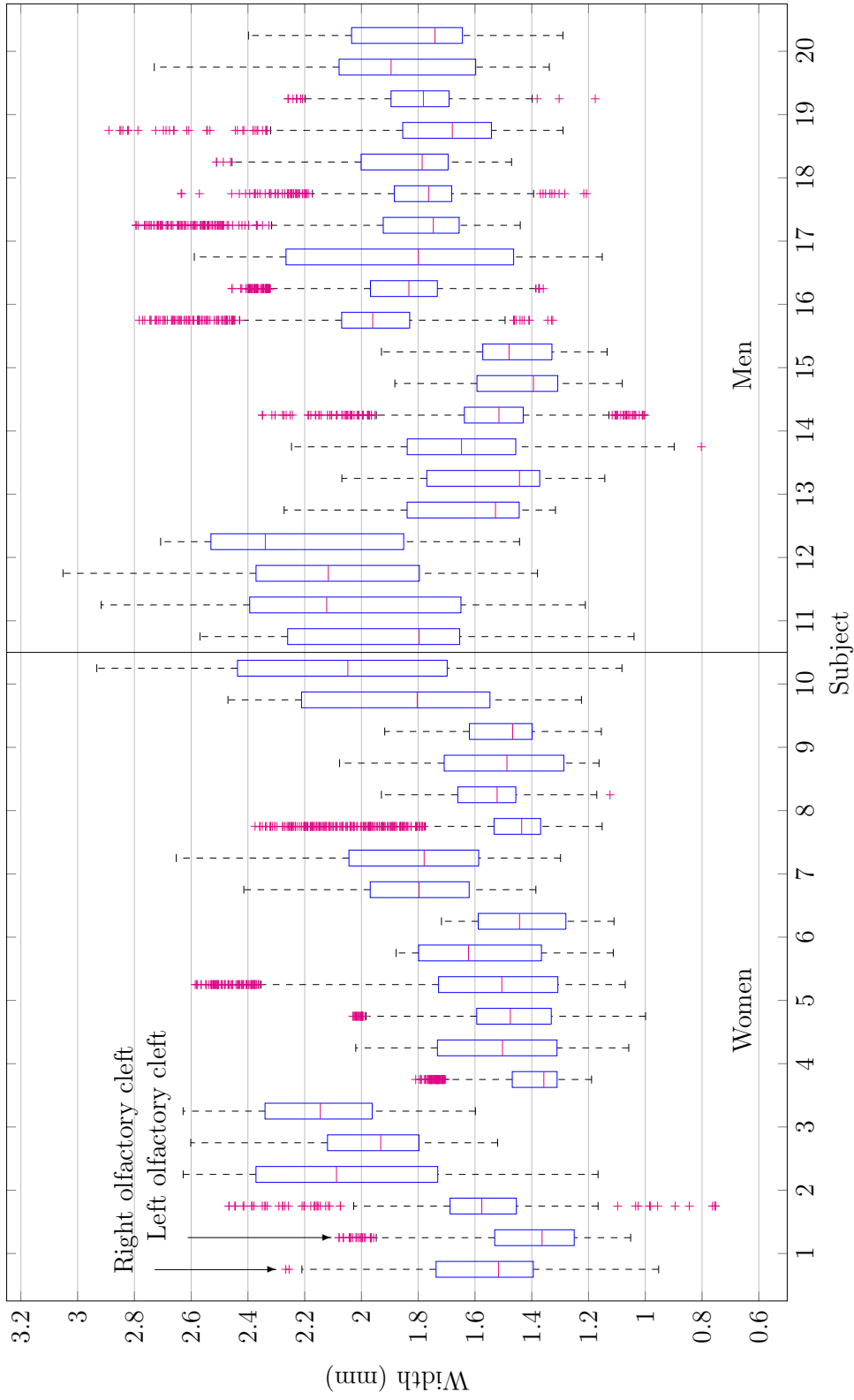
FIGURE 7. Boxplot that represents the width distribution for the olfactory clefts of each subject. The data represented on the right of each subject number represents the measurements for the right olfactory cleft, and the left ones represent data that are related to the left olfactory cleft.

TABLE 1. Statistics about the width of the olfactory cleft, established from the 20 subjects.

Measure	Minimum	Maximum	Mean	Median	Standard deviation
Value (mm)	0.75	3.05	1.74	1.67	0.35

(a)   **(b)**
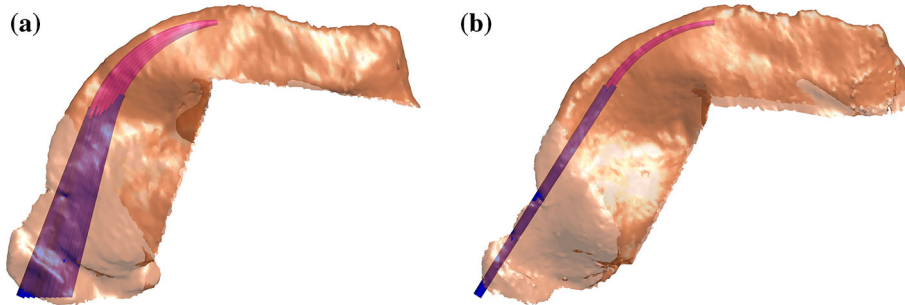
FIGURE 8. (a) High (subject n°2) and (b) low (subject n°3) number of solutions for the navigation section, with 950 and 3 solutions, respectively. All admissible solutions are superimposed, which outlines the impact of robot/nasal cavity pose adjustment.

TABLE 2. Collision test results for the navigation and exploration sections.

		Curvature of the navigation section c_2 (mm^{-1})		
Subject	Nasal cavity	0.03	0.04	0.05
1	Right	–	28.7–28.7/30.4–30.4/10.0–10.0	–
	Left	3.1–31.8/31.5–59.6/4.0–16.0	–	–
2	Right	10.9–32.7/34.3–58.0/1.0–12.0	29.1–42.5/23.3–37.1/1.0–13.0	36.9–46.0/19.8–26.9/1.0–13.0
	Left	17.5–30.0/41.4–52.7/4.0–7.0	–	–
3	Right	36.6–36.6/30.3–30.3/8.0–8.0	44.4–45.4/22.3–23.5/1.0–10.0	–
	Left	–	–	–
4	Right	–	–	–
	Left	23.5–28.2/37.4–41.1/1.0–1.0	–	–
5	Right	14.3–14.3/43.7–43.7/3.0–3.0	23.7–31.8/25.8–33.5/2.0–3.0	29.3–32.0/25.2–27.1/3.0–3.0
	Left	22.1–29.6/31.1–39.7/5.0–5.0	32.5–35.6/24.6–28.6/4.0–9.0	–
6	Right	–	32.2–41.5/22.9–29.9/1.0–19.0	39.9–45.0/18.7–22.8/1.0–25.0
	Left	26.9–29.4/35.6–38.6/2.0–6.0	–	–
7	Right	–	28.3–34.7/26.9–33.0/1.0–20.0	–
	Left	21.0–24.3/37.6–40.4/3.0–3.0	30.5–35.7/25.4–30.4/1.0–6.0	–
8	Right	14.4–26.5/36.3–49.1/3.0–8.0	27.9–37.3/24.1–34.3/3.0–10.0	34.8–42.5/18.2–26.2/3.0–11.0
	Left	12.9–20.3/41.2–49.5/1.0–11.0	27.1–36.4/24.2–34.3/1.0–13.0	34.1–41.8/18.2–26.3/1.0–15.0
9	Right	–	23.7–27.3/28.2–32.1/4.0–5.0	34.0–35.0/21.1–21.8/4.0–5.0
	Left	–	–	36.9–38.7/19.3–20.3/3.0–3.0
10	Right	–	15.7–25.6/24.9–35.6/1.0–15.0	23.3–28.9/21.9–27.1/1.0–7.0
	Left	–	18.9–25.9/24.8–32.4/2.0–6.0	29.0–33.1/20.7–23.0/2.0–6.0
11	Right	4.6–19.7/41.2–57.8/3.0–11.0	22.4–34.0/29.4–40.8/5.0–28.0	31.7–41.2/18.8–27.4/3.0–24.0
	Left	–	27.6–30.8/28.3–31.5/4.0–4.0	–
12	Right	–	23.3–33.0/26.4–34.6/3.0–9.0	29.4–40.7/18.7–27.9/2.0–9.0
	Left	–	–	35.9–41.8/18.7–22.6/1.0–9.0
13	Right	–	16.6–27.7/23.6–34.7/1.0–10.0	23.9–35.0/16.6–26.8/1.0–11.0
	Left	–	14.5–29.8/21.9–36.8/4.0–9.0	22.5–30.9/21.7–27.5/4.0–11.0
14	right	4.6–27.8/35.2–59.0/3.0–11.0	25.9–36.0/26.4–35.1/5.0–5.0	39.2–41.5/21.3–23.2/5.0–13.0
	Left	16.5–29.3/33.6–45.0/7.0–11.0	31.8–35.9/25.6–29.1/5.0–16.0	37.4–38.3/22.6–23.1/5.0–5.0
15	Right	–	–	–
	Left	–	–	–
16	Right	–	18.0–34.8/25.7–39.1/4.0–7.0	–
	Left	6.6–29.7/30.8–51.9/4.0–6.0	24.1–41.9/19.6–31.4/5.0–6.0	44.3–44.5/16.3–16.4/5.0–5.0
17	Right	–	–	17.9–24.6/24.5–31.7/6.0–9.0
	Left	–	8.9–24.8/27.2–42.2/3.0–3.0	21.4–21.9/28.1–28.6/1.0–3.0

TABLE 2. continued.

Subject	Nasal cavity	Curvature of the navigation section c_2 (mm^{-1})		
		0.03	0.04	0.05
18	Right	–	19.9–24.9/26.2–33.5/1.0–6.0	27.9–29.1/22.9–23.8/2.0–9.0
	Left	–	22.3–23.7/26.9–28.7/4.0–12.0	26.9–28.4/22.0–24.3/6.0–14.0
19	Right	–	30.5–31.7/24.3–25.0/7.0–7.0	–
	Left	–	–	–
20	Right	–	–	–
	Left	–	30.0–39.9/22.1–27.9/8.0–9.0	36.2–44.6/16.9–20.8/8.0–10.0

Geometries of the navigation and exploration sections depending on the curvature c_2 of the navigation section, presented as follows for each nasal cavity: $\min(l_1) - \max(l_1)/\min(l_2) - \max(l_2)/\min(l_3) - \max(l_3)$. No value is reported if no contactless solution is identified for the navigation section, which means that the exploration section could not be computed.

number of sections would increase the number of tubes, and therefore cause issues with the thickness of their walls. The explorable ratio represents a significant portion of scanned olfactory cleft, in an area where the OE is known to be present and dense.[27]

DISCUSSION

In this paper, we have elaborated new anatomical data of the nasal cavity, with 3D reconstructions and extraction of relevant estimators to characterize their shape as well as variations on 20 subjects (i.e., 40 nasal cavities). The constraints to non-invasively reach the olfactory cleft, an unexplored area of the human anatomy, are now available. The full 3D data, that are meshes with the stl file format, are accessible upon request using the provided link,[1] and can be used by properly citing this paper. The detailed analysis allowed in a second step the extraction of navigation sections for the deployment of a CTR, taking into account subject inter-variability. It is shown that a navigation section composed of simply 2 links is suitable to reach the entry of the olfactory clefts. The obtained inspection rate (90% of the subjects) as well as the explored ratio (35% of the length of the olfactory clefts) for a navigation section curvature of 0.04 mm^{-1} are suitable for medical purposes, on selected subjects. These results are all the more interesting given that no conventional instrument can even reach the olfactory cleft today. The development of such robot is thus of high interest. It opens the way to *in situ* optical biopsies of the OE, that can have a significant impact on the understanding of olfactory mechanisms and related neuroscience applications. Future work will be focused on the technical development of a compact robot, based on the obtained navigation and exploration section parameters. Also,

the presented methodology will be considered for other scenarios in ENT surgery, and potentially broader application fields. Finally, its extension will be considered to variable-curvature segments, that can be now designed for instance with smart materials.

CONFLICT OF INTEREST

No benefits in any form have been or will be received from a commercial party related directly or indirectly to the subject of this manuscript.

REFERENCES

[1]Aarli, J. A., T. Dua, A. Janca, and A. Muscetta. Neurological Disorders: Public Health Challenges. Geneva: World Health Organization, 2006, pp. 32.
[2]Amorim, P., T. Moraes, J. Silva, and H. Pedrini. In-Vesalius: An interactive rendering framework for health care support. In: Advances in Visual Computing, 2015, vol. 9474, pp. 45–54.
[3]AGILTRON. Miniature oct fiber probe. http://www.agiltron.com/PDFs/Miniature.
[4]Bergeles, C., A. H. Gosline, N. V. Vasilyev, P. J. Codd, P. J. del Nido, and P. E. Dupont. Concentric tube robot design and optimization based on task and anatomical constraints. *IEEE Trans. Robot.* 31(1):67–84, 2015.
[5]Bojsen-Moller, F. and J. Fahrenkrug. Nasal swell-bodies and cyclic changes in the air passage of the rat and rabbit nose. *J. Anat.* 110:25, 1971.

[1]http://projects.femto-st.fr/projet-nemro/contact.

[6]Bruyas, A., F. Geiskopf, and P. Renaud. Toward unibody robotic structures with integrated functions using multi-material additive manufacturing: case study of an MRI-compatible interventional device. In: IEEE/RSJ International Conference on Intelligent Robots and Systems (IROS), 2015, pp.1744–1750.

[7]Bui, N. L., S. H. Ong, and K. W. C. Foong. Automatic segmentation of the nasal cavity and paranasal sinuses from cone-beam CT images.*Int. J. Comput. Assist. Radiol. Surg*. 10(8):1269–1277, 2015.

[8]Burgner-Kahrs, J., D. C. Rucker, and H. Choset. Continuum robots for medical applications: a survey. *IEEE Trans. Robot*. 31(6):1261–1280, 2015.

[9]Burgner, J., P. J. Swaney, R. Lathrop, K. D. Weaver, R. J. Webster *et al*. Debulking from within: a robotic steerable cannula for intracerebral hemorrhage evacuation. *IEEE Trans. Biomed. Eng*. 60(9):2567–2575, 2013.

[10]Butler, E. J., R. Hammond-Oakley, S. Chawarski, A. H. Gosline, P. Codd, T. Anor, J. R. Madsen, P. E. Dupont, and J. Lock. Robotic neuro-endoscope with concentric tube augmentation. In: IEEE/RSJ International Conference on Intelligent Robots and Systems (IROS), 2012, pp.2941–2946.

[11]Cignoni, P., M. Callieri, M. Corsini, M. Dellepiane, F. Ganovelli, and G. Ranzuglia. MeshLab: an open-source mesh processing tool. In: Sixth Eurographics Italian Chapter Conference, 2008, pp.129–136.

[12]Costanzo, R. M. Regeneration of olfactory receptor cells. *Ciba Found. Symp*. 160:233–248, 1991.

[13]Doty, R. L. Olfactory dysfunction in Parkinson disease. *Nat. Rev. Neurol*. 8(6):329–339, 2012.

[14]Dryer, L. and P. Graziadei. Influence of the olfactory organ on brain development. *Perspect. Dev. Neurobiol*. 2(2):163–174, 1994.

[15]Dupont, P. E., J. Lock, B. Itkowitz, and E. Butler. Design and control of concentric-tube robots. *IEEE Trans. Robot*. 26(2):209–225, 2010.

[16]Elwany, S., A. Medanni, M. Eid, A. Aly, A. El-Daly, and S. Ammar. Radiological observations on the olfactory fossa and ethmoid roof. *J. Laryngol. Otol*. 124(12):1251–1256, 2010.

[17]Escada, P. A., C. Lima, and J. M. da Silva. The human olfactory mucosa. *Eur. Arch. Oto-Rhino-Laryngol*. 124(12):1251–1256, 2010.

[18]Flood, D. G. and P. D. Coleman. Neuron numbers and sizes in aging brain: comparisons of human, monkey, and rodent data. *Neurobiol. Aging* 9:453–463, 1988.

[19]Gilbert, H. B., J. Neimat, and R. J. Webster. Concentric tube robots as steerable needles: achieving follow-the-leader deployment. *IEEE Trans. Robot*. 31(2):246–258, 2015.

[20]Gladwin, K. and D. Choi. Olfactory ensheathing cells: part Icurrent concepts and experimental laboratory models. *World Neurosurg*. 83(1):114–119, 2015.

[21]Godoy, M. D. C. L., R. L. Voegels, F. de Rezende Pinna, R. Imamura, and J. M. Farfel. Olfaction in neurologic and neurodegenerative diseases: a literature review. *Int. Arch. Otorhinolaryngol*. 19(2):176–179, 2015.

[22]Gopinath, B., K. J. Anstey, A. Kifley, and P. Mitchell. Olfactory impairment is associated with functional disability and reduced independence among older adults. *Maturitas* 72(1):50–55, 2012.

[23]Gosline, A. H., N. V. Vasilyev, E. J. Butler, C. Folk, A. Cohen, R. Chen, N. Lang, P. J. Del Nido, and P. E. Dupont. Percutaneous intracardiac beating-heart surgery using metal mems tissue approximation tools. *Int. J. Robot. Res*. 31(9):1081–1093, 2012.

[24]Hudson, T. C., M. C. Lin, J. Cohen, S. Gottschalk, and D. Manocha. V-COLLIDE: accelerated collision detection for VRML. In: Proceedings of the second symposium on Virtual reality modeling language, 1997, pp.117–123.

[25]Jones, B. A. and I. D. Walker. Kinematics for multisection continuum robots. *IEEE Trans. Robot*. 22(1):43–55, 2006.

[26]Kalmey, J. K., J. Thewissen, and D. E. Dluzen. Age-related size reduction of foramina in the cribriform plate. *Anat. Record* 251(3):326–329, 1998.

[27]Kavoi, B. M. and H. Jameela. Comparative morphometry of the olfactory bulb, tract and stria in the human, dog and goat. *Int. J. Morphol*. 29(3):939–946, 2011.

[28]Lavoie, J., P. Gass Astorga, H. Segal-Gavish, Y. Wu, Y. Chung, N. Cascella, A. Sawa, and K. Ishizuka. The olfactory neural epithelium as a tool in neuroscience. *Trends Mol. Med*. 23(2):100–103, 2017.

[29]Lorensen, W. E. and H. E. Cline. Marching cubes: a high resolution 3D surface construction algorithm. *SIGGRAPH Comput. Graph*. 21(4):163–169, 1987.

[30]Moench, T., R. Gasteiger, G. Janiga, H. Theisel, and B. Preim. Context-aware mesh smoothing for biomedical applications. *Comput. Graph*. 35(4):755–767, 2011.

[31]Moon, C., S. J. Yoo, and H. S. Han. Smell, Encyclopedia of the Neurological Sciences, 2nd ed. Cambridge: Academic Press, 2014, pp. 216–220.

[32]Renevier R., Tamadazte B., Rabenorosoa K., Tavernier L., and Andreff N. Endoscopic laser surgery: design, modeling and control. *IEEE/ASME Trans. Mech*. 22(1):99–106, 2017.

[33]Robert J. Webster, I. and B. A. Jones. Design and kinematic modeling of constant curvature continuum robots: a review. *Int. J. Robot. Res*. 29(13):1661–1683, 2010.

[34]Savvateeva, D. M., C. Güldner, T. Murthum, S. Bien, A. Teymoortash, J. A. Werner, and M. Bremke. Digital volume tomography (DVT) measurements of the olfactory cleft and olfactory fossa. *Acta Oto-Laryngol*. 130(3):398–404, 2010.